ACS APPLIED MATERIALS & INTERFACES

Research Article

www.acsami.org

Molecular Insights into the Electric Double Layers of Ionic Liquids on Au(100) Electrodes

Maolin Sha,[†] Qiang Dou,[‡] Fabao Luo,[†] Guanglai Zhu,[∥] and Guozhong Wu*,[‡]

[†]Department of Chemistry and Chemical Engineering, Hefei Normal University, Hefei 230061, China

[‡]Shanghai Institute of Applied Physics, Chinese Academy of Sciences, Shanghai 201800, Box 800-204, China

[∥]Institute of Atomic and Molecular Physics, Anhui Normal University, Wuhu 241000, China

Supporting Information

ABSTRACT: The electric double layer structure and differential capacitance of single crystalline Au(100) electrodes in the ionic liquid 1-butyl-3-methyl-imidazolium hexafluorophosphate are investigated using molecular dynamics simulations. Results show strong adsorption on the electrode surface. The potential of zero charge (pzc) and maxima of differential capacitance are strongly dependent on the adsorption layer structure. At potentials near the pzc, cations and anions adjacent to the electrode surface are coadsorbed on the same screening layer. This strong adsorption layer results in overscreening effects on the compact layer and induces both a bell-shaped differential capacitance curve and a positive pzc. Moreover, the potential required for transition from overscreening to overcrowding is about 4.0 V. This transition potential may be attributed to the higher interaction energy between the Au(100) electrode and ions compared with the binding energy in our cation−anion system.

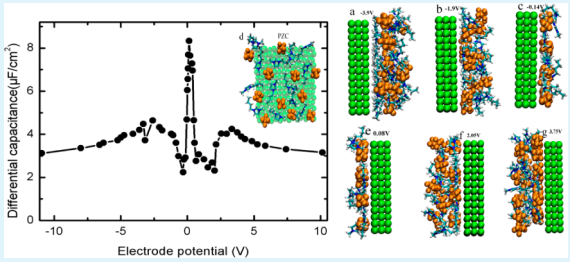

KEYWORDS: *ionic liquid, electric double layer, molecular dynamics simulation, adsorption*

1. INTRODUCTION

Room-temperature ionic liquids[1,2] (ILs) are fascinating molten salts and promising electrolyte candidates.[3] The characteristics of ILs include a broad electrochemical window, good ionic conductivity, nonflammability, and low vapor pressure. These characteristics contribute to the potential applications of ILs in fuel cells, supercapacitors, and other electrochemical devices. For applications in these fields, ILs must come into contact with charged solid surfaces or be transported into charging and discharging microporous cells.[4−7] Hence, a more detailed understanding of the molecular level description of ILs on electrode surfaces is important, particularly in applications that use electrolyte structures to store energy. Further analysis of IL microlevel behaviors at electrodes and electric double layer (EDL) structures is beneficial for designing and optimizing different devices to achieve optimum performance.

ILs are governed by a complex combination of van der Waals, Coulomb, dipole, and hydrogen bond interactions; this complex combination is rarely observed in other materials.[8] As room-temperature molten salts, ILs constitute infinite concentrations of electrolytes. The IL/electrode system is difficult to depict via conventional electrochemical theories that depend on dilute-solution approximation. Addressing these questions through experiments is difficult because it is lack of direct microscopic techniques and appropriate samples to observe the molecular scale dependence of the electric potential change.[4,9] Considering the potential technological applications of ILs in electrochemical devices, many scientists have conducted electrochemical experiments on the IL/electrode system to hypothesize the possible EDL structures. These vast amounts of experiments all underlie the voltage dependence of interfacial capacitance and these capacitance−potential curves are puzzling, that is, a weak dependence of electrode potential, dependence on the IL purification procedure, the reference electrode stability, the surface of electrode materials, and the methods for extracting capacitance data from experiments.[10−24] Electrochemical studies are so rarely performed on genuinely clean and structurally well-defined crystal surfaces, particularly in electrode materials, that extensive quality differences may be observed among available reports. Using polycrystalline electrodes in these studies increases the complexity of precise analysis and theoretical modeling. Polycrystalline surfaces lack identical arrangements of the ionic adsorption layer, which could contain abundant information on the different EDL structures of single crystalline surfaces. Several scholars recently conducted electrochemical experiments using combined in situ scanning tunnelling microscopy and in situ atomic force microscopy on completely single crystalline metal electrodes and extremely pure ILs.[19−29] Unfortunately, the important experiment results of these studies lack reasonable understanding at the molecular scale.

Received: April 24, 2014
Accepted: July 14, 2014
Published: July 21, 2014

From the theoretical point of view, the IL/solid electrode interface has been poorly investigated until very recently.[30−50] The experimental results of bell-shaped or camel-shaped differential capacitance curves in ILs with one or several maxima are evidently different from the U-shaped curves typically observed in dilute electrolytes. Thus, these and similar results cannot be solely described using standard Gouy−Chapman−Stern theory. Kornyshev[31−33,45] recently developed a new mean-field-based theory that qualitatively describes the effects related to the bell-shaped or camel-shaped differential capacitance curves as well as lattice saturation in the IL/electrode systems. Oldham[42] further demonstrated that the same qualitative description can be obtained by replacing the solvent−ion viewpoint with cation−anion exchange in a conventional Gouy−Chapman−Stern model. Lamperski et al.[46,47] applied atomistic simulations and modified Poisson−Boltzmann theory to reveal that a bell-shaped differential capacitance can be promoted by high density and high thermal energy. By contrast, the custom U-shaped differential capacitance can be obtained by low density and low thermal energy. Despite the improved understanding such findings provide, however, these semiphenomenological theories omit many important details of the chemical interactions. Such details include simple spherical models or ionic sizes and descriptions of the specific adsorption interaction between the electrode surface and ions. In contrast to these semi-phenomenological theories, the majority of recent atomistic simulation studies on IL/electrode systems have focused on simple models designed to represent generic features of flat electrode surfaces and ILs.[34−41] A report by Tazi et al.[48] discussed the EDL structures of inorganic salt LiCl to represent common IL on single crystalline electrode surfaces. However, no study has yet simulated a real IL/single crystalline metal electrode system nor discussed possible molecular-scale EDL structures in comparison with single crystalline metal electrode experimental results.

In the present work, we use atomistic molecular simulations to study the IL 1-butyl-3-methylimidazolium hexafluorophosphate ($BmimPF_6$) on a Au(100) electrode surface in the molecular scale. $BmimPF_6$ was selected because of its popular applications in electrochemical device, wide electrochemical window, and high stability. The Au(100) electrode surface was chosen because it represents a typical single crystalline metal electrode and has been examined in several electrochemical experiments.[19−23] We investigate variations in the EDL structures and differential capacitance as functions of electrode potential. Unlike in previous reports on suggested EDL structures, our simulations reveal that $BmimPF_6$ on the Au(100) electrode exhibits a bell-shaped differential capacitance. This curve is highly dependent on intensive adsorption interactions between the metal electrode surface and ions. This specific adsorption interaction results in overscreening effects and a positive potential of zero charge (pzc). Molecular dynamics simulations of this IL/single-crystalline metal electrode have allowed us to gain molecular insight into the complex EDL structures for real ionic liquids and single-crystalline metal electrodes, especially in ion size and specific adsorption interactions between electrode surfaces.

2. METHODOLOGY AND SIMULATION DETAILS

The $[Bmim][PF_6]$ molecule was treated as a systematic all-atom OPLS-AA force field[51] as developed by Lopes et al.,[52] which was successfully used in our previous simulations.[53,54] The model system consisted of 314 $[Bmim][PF_6]$ molecules and two Au electrode surfaces in a tetragonal box. The electrodes included 588 fixed Au atoms arranged in a face-centered cubic (fcc) structure with the (100) surface exposed to the IL. The dimensions of the cell were 28.56 Å in the x and y directions and 125.92 Å between the innermost layers of electrode atoms along the z direction. A 100 Å slab of vacuum was inserted into the cell to separate each electrode from the next periodic imagine in the z direction and eliminate artifacts from the periodicity of the simulation cell.[55,56] The 314 $[Bmim][PF_6]$ molecules of bulk phase IL were simulated first for 2 ns in the isothermal−isobaric ensemble to ensure full equilibration. The equilibrated bulk-phase IL was inserted within the electrodes aligned in the z direction (Figure 1).

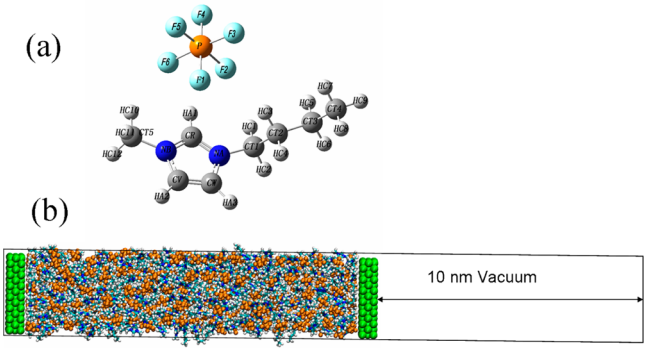

Figure 1. (a) Molecular structure of $[Bmim][PF_6]$ with atomic labels. (b) The schematic configuration of the simulation unit cell.

Here, the bulk-phase IL was not in contact with the electrode surfaces; the IL was approximately 0.3 nm away from the surfaces. A constant charge method was used to simulate the electrode charge, in which a constant and uniform charge was assigned to each Au(100) surface atom. A complete model should consider the electron density on the Au electrode surface and the surface electron response to the EDL. However, a simplified approach to constant charge allocation provides valuable insights into the EDL structures of the IL on the single crystalline metal electrode; this approach has been applied well in other electrolyte/metal electrode systems.[57−59] In our simulation, each Au atom within the first layer of the Au(100) anode surface (facing the bulk-phase IL) was allocated with a quantitative positive charge in our simulation systems. The system was neutralized by assigning the same value of negative charge to the Au atoms of the Au(100) surface in the cathode. The surface charge density σ can be obtained by summing all of the atom charge within the Au(100) electrode and then dividing the electrode area. Simulation trajectories were also obtained for 25 applied voltages between Au(100) electrodes. At each applied voltage, EDLs at the negative and positive electrodes were analyzed separately, and 50 EDL structure data were obtained. Surface van der Waals (vdW) interactions of Au(100) atoms were represented by a 6−12 Lennard−Jones potential with the cross-sectional parameters σ = 0.33124 nm and ε = 22.1333 kJ/mol in our simulation. These parameters, which were developed by Heinz et al.,[60] can accurately reproduce the properties of the fcc Au metal surface.

Periodic boundary conditions were applied in all directions. In all simulations, bond length was constrained using the lincs algorithm. The Lennard−Jones interaction cutoff was set to 1.2 nm. Long-range Coulomb interactions were addressed using the particle mesh Ewald method with a cutoff of 1.2 nm and a grid spacing of 0.12 nm. The Au(100) electrode surfaces were fixed in our simulations. The melting point of the bulk $[Bmim][PF_6]$ at ambient pressure (0.1 MPa) was estimated to be approximately 279 K.[61] Thus, a series of simulations was performed at a fixed temperature of 300 K using Gromacs 4.3[62,63] to ensure that the IL remained in the liquid state. A Berendsen thermostat was used to mimic weak coupling, and cations and anions were separated into two heat baths with temperature coupling constants of 0.1 ps. All systems were run for 1 ns at 1000 K and then annealed from 1000 to 300 K in three stages: 1 ns at 800 K, 1 ns at 600

K, and 1 ns at 300 K. All configurations were subsequently equilibrated in the NVT simulation for 10.0 ns followed by a trajectory of duration of 10.0 ns with a time step of 2 fs.

3. RESULTS AND DISCUSSION

3.1. Differential Capacitance and Integral Capacitance. The differential capacitance and integral capacitance

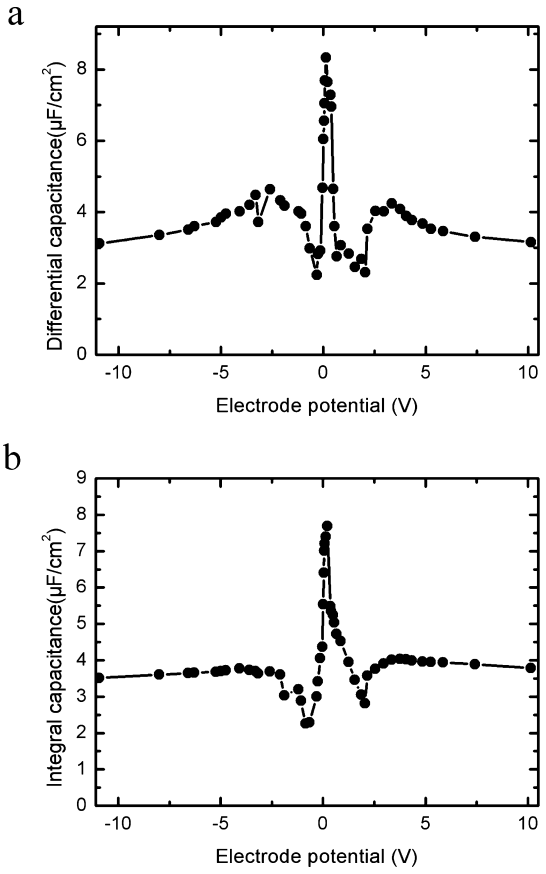

Figure 2. Differential capacitance and integral capacitance as a function of electrode potential relative to the pzc. (a) Differential capacitance. (b) Integral capacitance.

(C) is plotted as a function of the EDL potential drop (U) in Figure 2. To obtain the differential capacitance and integral capacitance, we first calculate the total Poisson potential: $\phi(z)$. The Poisson potential can be obtained by integrating the Poisson equation $d^2\phi(z)/dz^2 = -\rho(z)/\varepsilon_0$ for the measured charge profile along the z-axis: $\rho(z)$. The potential drop within the electric double layer can be calculated by the equation $U = \phi_{electrode} - \phi_{bulk} - pzc$. The pzc can be determined from the difference between the Poisson potential on the electrode and that in the bulk for simulations on uncharged electrode surfaces (Details of the differential capacitance, integral capacitance and pzc calculation are shown in the Supporting Information). The pzc in our simulation system was 0.45 V, which is very different from the negative pzc obtained on a graphite electrode surface.[35] The Au atoms within the electrode have a higher surface atom density and stronger van der Waals forces than the carbon atoms in graphite. Hence, high affinity toward cations is produced because the cation possesses a large imidazolium ring and a long alkyl chain. This finding also coincides with the neutron reflectometry experiment,[29] in which the long alkyl chain cation of IL was specific adsorbed even at a positively

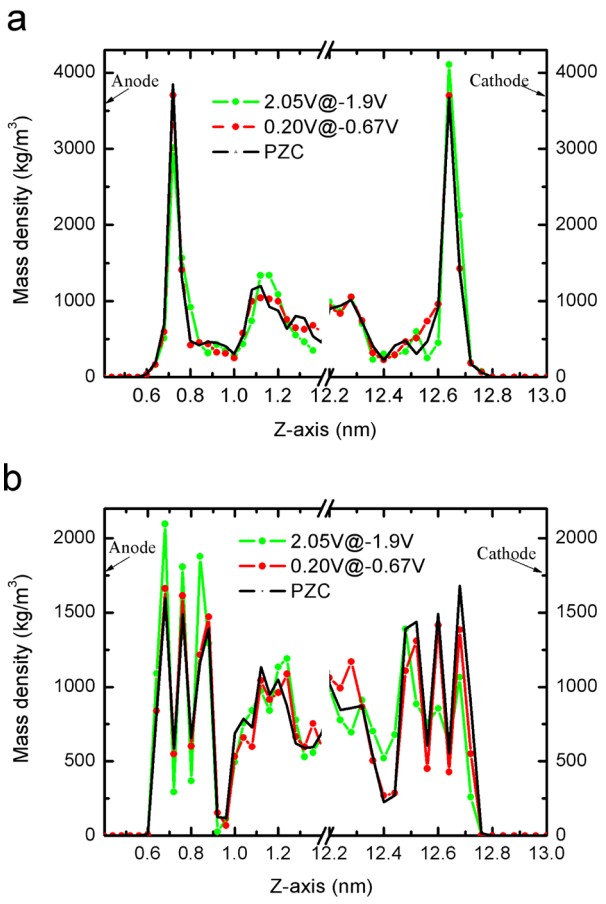

Figure 3. Separated ion mass density profiles for $BmimPF_6$ at different applied electrical potential. The potentials were shown for three different values of the absolute values of the charge density of electrodes, the green line corresponds to 1.53 $\mu C/cm^2$, the red line corresponds to 0.58 $\mu C/cm^2$, and the black line corresponds to the uncharged electrodes. The applied Poisson potentials at the anode and the cathode were all relative to pzc and labeled separately in the figure. The anode and the cathode were separately placed at x = 0.4 nm, and x = 13.0 nm. (a) The mass density profile of cation. (b) The mass density profile of anion.

charged Au electrode. It illustrates that the selection of different electrode surfaces and ILs may induce different adsorption formations and alterable differential capacitance curves on electrode surfaces.

The differential capacitances and the integral capacitance illustrated in Figure 2 both indicate a bell-shaped curve with two declining wings. These capacitance curves exhibit maxima ranging from +0.1 V to +0.2 V and two minima ranging from −0.2 to −0.8 V and from +1.2 V to +2.0 V. These data of differential capacitance are very similar to the experimental results of the same IL on a Au(100) electrode[22] (i.e., 4−8 $\mu F/cm^2$). Moreover, this bell-shaped curve is similar to the electrochemical observation of the IL on single crystalline Au electrodes.[20,21,23,24] Our analysis on mechanism underlying the EDL structures with electrode potentials focuses on differential capacitance, since differential capacitance is the most important observable of electrochemistry experiments. Hence, we will focus on the discussion of differential capacitance in this work. The pzc in our simulations remarkably showed neither a minimum nor a maximum in differential capacitance. In conventional double-layer theories, a differential capacitance minimum is predicted at the pzc position. However, IL systems

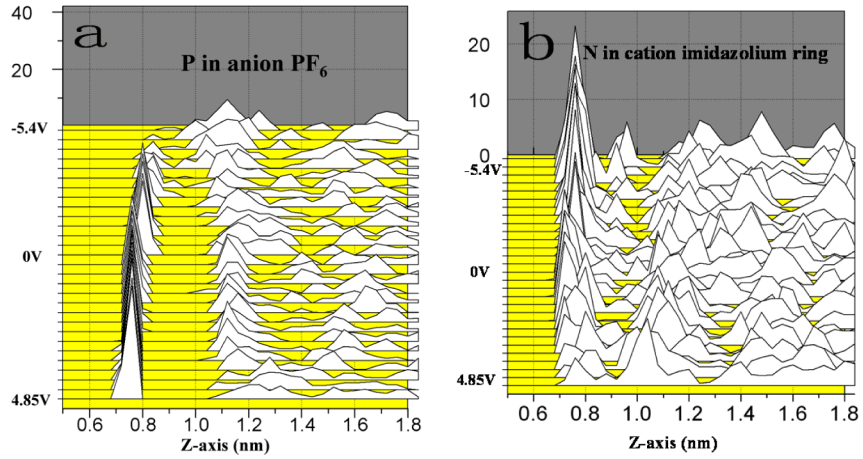

Figure 4. Atom number density as a function distance from the electrode surface for a series of electrical potential for (a) P in anion PF_6 and (b) N in cation Bmim. The potential are relative to pzc. Represented in the *x* axis are the distances from the electrode, in the *y* axis are the EDL potentials to pzc, and in the *z* axis are the actual values of the atom number density.

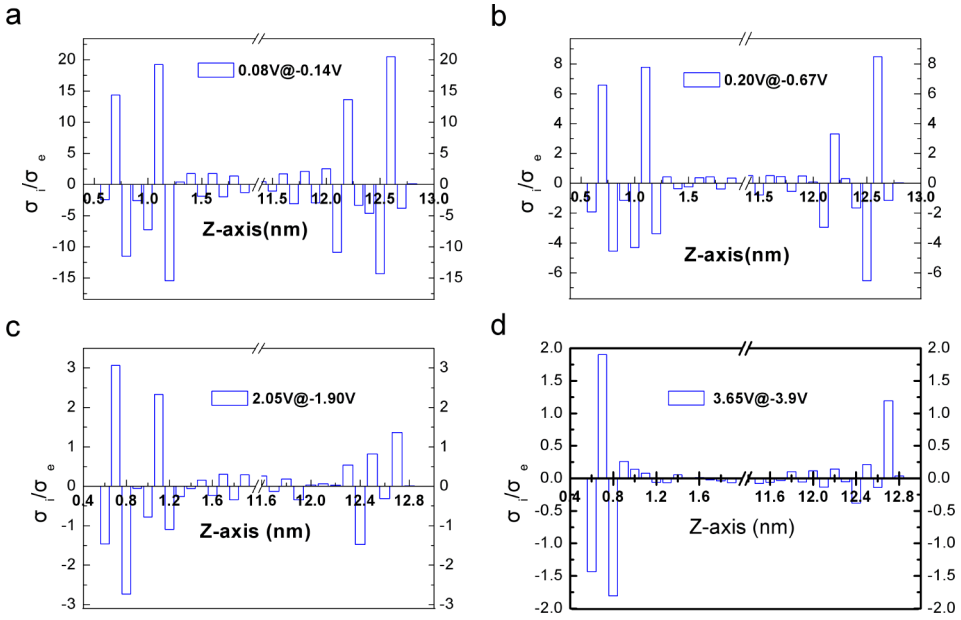

Figure 5. Sliced average charge density per unit surface area, scaled to the absolute value of the surface charge density of the electrode as a function of the applied Poisson potential. σ_e is the absolute values of the surface charge density of the electrode, (a) σ_e = 0.58 μC/cm^2, (b) σ_e = 1.53 μC/cm^2, (c) σ_e = 5.76 μC/cm^2, and (d) σ_e = 15.37 μC/cm^2. The charge density per unit surface area calculated for 0.1 nm thick slices. The anode and the cathode was separately placed at *x* = 0.4 nm, and *x* = 13.0 nm. The applied Poisson potentials at the anode and the cathode were all relative to pzc and labeled separately in the figure.

are very different from those systems described in conventional double-layer theories. Many experimental results clearly confirm that the position of the minimum or maximum of the differential capacitance in IL systems often does not correspond to the pzc.

The curve shape of the IL differential capacitance is another interesting finding. Kornyshev[31] discussed changes in the differential capacitance curve from camel-shape to bell-shape by introducing a lattice saturation parameter γ. In the Kornyshev mean-field model, the parameter γ describes a possible local concentration of the ions near the electrode surface and determines the curve shape. Lamperski et al.[46,47] further demonstrated that a bell-shaped curve of the differential capacitance can be obtained by increasing the local density of the hard sphere on the electrode surface. In our simulation system, the bell-shaped curve could be attributed to the high local density of ions near the electrode surface. Considering the strong affinity between the Au(100) electrode and the ions, a dense layer is induced on the electrode surface. This finding can be confirmed by the mass density profile of the ions (as shown in Figure S1, Supporting Information).

The cations and anions presents in the high-density layer near the electrode surface are located at the pzc. The mass density of ions on the Au(100) electrode is higher than that reported for the same IL on a graphite surface.[53] This finding shows specific adsorption interactions between the electrode and ions. Intensive adsorption interactions can be further confirmed by the interaction energies between the electrode surface and cations in the nearest dense layer. The cations in the nearest dense layer can be obtained by counting all of the cations in which the distance from the electrode surface is less than the first minimum value of the cation mass density

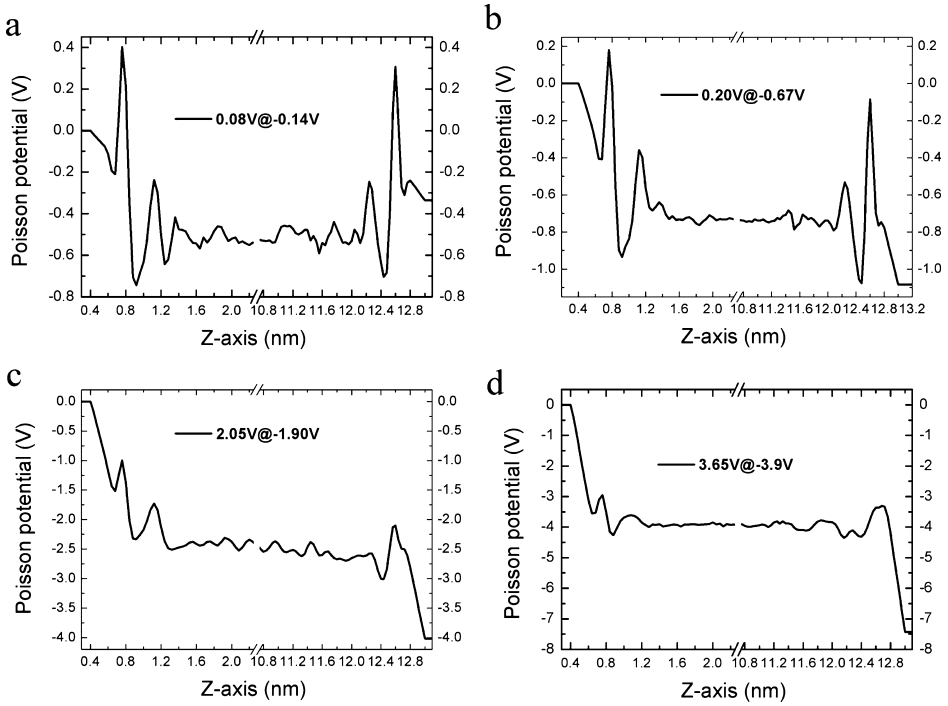

Figure 6. Poisson potential profiles across the simulation cell in z axis. The potentials were shown for four different values of the absolute values of the charge density of the electrodes, (a) 0.58 μC/cm^2, (b) 1.53 μC/cm^2, (c) 5.76 μC/cm^2, and (d) 15.37 μC/cm^2. The anode and the cathode was separately placed at x = 0.4 nm, and x = 13.0 nm. The applied Poisson potentials at the anode and the cathode were all relative to pzc and labeled separately in the figure.

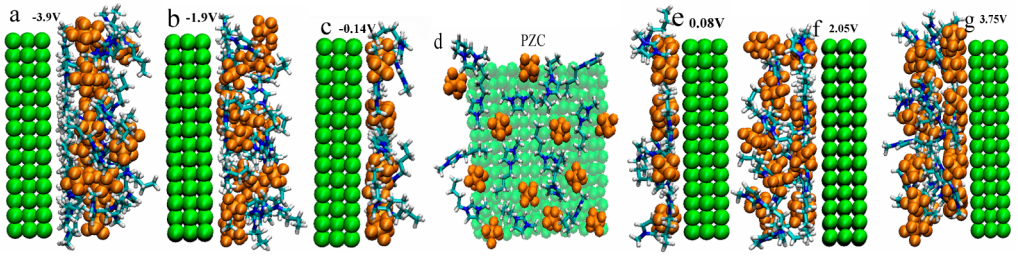

Figure 7. Representative snapshots of the EDL ion structures at the electrode for the different electrical potentials, (a) −3.9 V, (b) −1.9 V, (c) −0.14 V, (d) PZC, (e) 0.08 V, (f) 2.05 V, (g) 3.75 V. In these snapshots, we selected ions whose centers of mass were located within 1.0 nm from the electrode surface (a, b, f, g), except from the small electrical potential, were located within 0.5 nm (c−e). The Au electrode atoms are represented as green spheres, the anion atoms are represented as orange spheres and the cation atoms are represented as rod-shape.

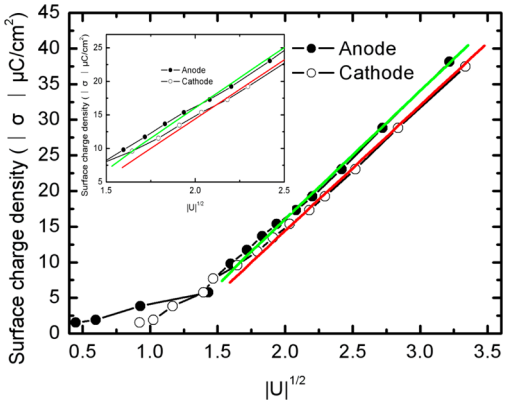

Figure 8. Dependence of the electrode surface charge density versus the square root electrical potential. The circle symbols are simulation data points, the straight lines are the fits to MD data. Inset shows the magnified part of the figure.

distribution at the electrode surface, that is, 0.6 nm (see the cation mass density distribution in Figure S1, Supporting Information). In the nearest dense layer, the interaction energy between each cation and the Au(100) electrode is −226.76 kJ/mol, which is higher than the cation−anion interaction energy −175.29 kJ/mol. This result implies that strong interactions between the Au(100) electrode and cations produce specific adsorption effects on the cations on the electrode surface and induce a bell-shaped differential capacitance curve.

3.2. Ion-Density Profile. To provide insights into the EDL structures in our electrode−electrolyte system, we examined the arrangement of electrolyte ions on the electrode under different electrical voltages. The ion density profiles of cation and anion along the z-axis (perpendicular to the electrode) are shown in Figure 3. The anode and cathode were placed at x = 0.4 nm and x = 13.0 nm, respectively.

The mass density of the cation exhibited a large dense peak at the anode and cathode surfaces, which indicates strong specific adsorption interactions between the electrode and

dx.doi.org/10.1021/am502413m | ACS Appl. Mater. Interfaces 2014, 6, 12556−12565

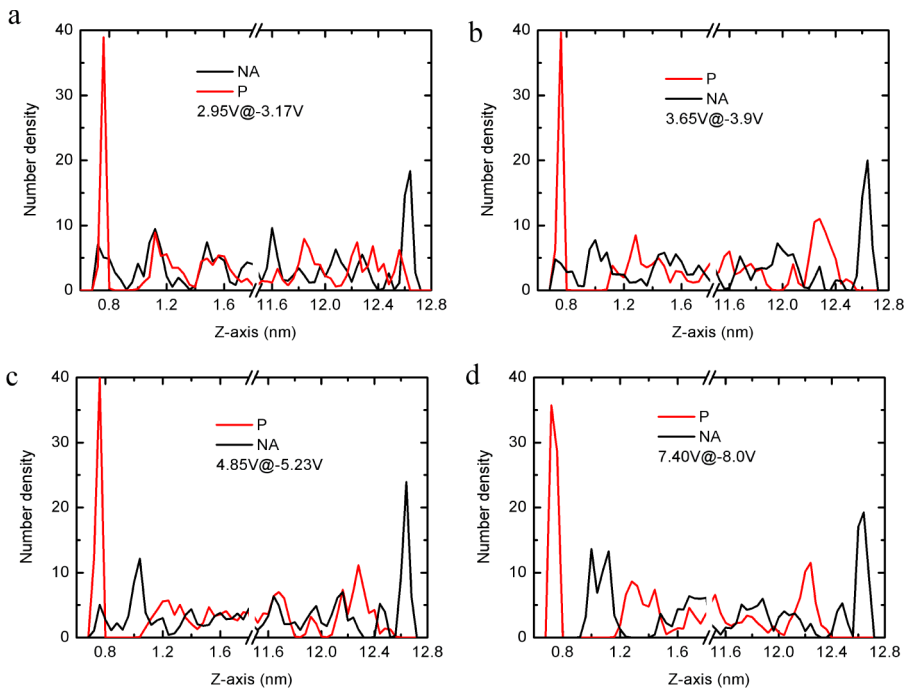

Figure 9. Atom number density as a function distance from the electrode surface for a series of electrical potential for P in anion PF_6 and N in cation Bmim. The potential are relative to pzc. (a) 2.95 V@−3.17 V. (b) 3.65 V@−3.9 V. (c) 4.85 V@−5.23 V. (d) 7.40 V@−8.0 V.

cations. From the pzc to a small electrical voltage (i.e., a small surface charge density on the electrode), the cation density peaks retain their positions and heights because of specific adsorption interactions with the electrode surface. Only under a high electrical voltage do the cation density peaks apparently decrease at the anode and increase at the cathode. By contrast, the anion density peaks ascend slightly at the anode and gradually descend at the cathode while slowly shifting away from the cathode under a change in electrical voltage. These results show that near the pzc or under a small surface charge density, the electrical voltage difference is mainly derived from the compact layer structure composed of the modified anion layer and the unmodified cation adsorption layer.

For a small positive surface charge density at the anode, the anode surface hardly rearranges cations and produces enough surface sites to attract additional bulk anions into the compact layer. At the cathode, the anions within the compact layer are easily expelled from the compact layer, which produces a compact layer with a large net positive charge. Only a large electrode surface charge can change a compact layer in the cation and anion layers. The differential capacitance can be depicted by $C = d\sigma/d\varphi$, which means that the smaller the value of $d\varphi$ induced by the unit surface charge density $d\sigma$, the larger the value of the differential capacitance. Hence, at a small positive surface charge density σ, the $d\varphi$ contributed by an increase in the anion layer density peak is relatively smaller at the anode than the $d\varphi$ produced by both an anion layer increase and cation layer decrease under a high surface charge density. For example, the potential difference $\Delta\varphi$ at the anode is 0.35 V for surface charge density differences from 0 $\mu C/cm^2$ to 1.92 $\mu C/cm^2$. By contrast, under the same charge density difference from 3.84 $\mu C/cm^2$ to 5.76 $\mu C/cm^2$, the potential difference $\Delta\varphi$ is 1.20 V. This finding may explain the vertex of the bell shape produced in our system by the differential capacitance under a small positive electrical voltage. Our results also coincide with Kornyshev's EDL theory,[31] in which larger cation sizes in the EDL result in a shift in the capacitance maximum toward positive potentials.

Our simulation results further show the asymmetric profile of the anion density peak locations at the cathode and anode (i.e., the anion density peak shifts away from the cathode and remains at the same position at the anode when the electrode surface charges are opposite in sign). At the cathode, the drifting location of the anion density peak indicates a relative increase in cation density peak in the compact layer. This increase results in enlarged EDL screening at the cathode, which produces a high electrical potential difference and low differential capacitance. This finding can explain why the minimum of the differential capacitance curve locate at a small negative electrical voltage range, that is, around −0.8 V at the cathode. This drifting behavior of the anion density peak at the cathode can be confirmed by the atomic number density profiles in the EDL regions, which are functions of the distance from the electrode surface for the entire range of electrode potentials investigated (Figure 4). The location of the number density peak *P* (in anion PF_6) is gradually moves away from the electrode under negative electrical potentials, whereas the number density peak *N* (in cation Bmim) shows a minimal change in location over the entire electrode potential range.

3.3. Electric Double Layer Structures. To obtain a more detailed picture of the relationship between the EDL structures and the differential capacitance as a function of the applied electrical potential, we sliced the slab between the electrodes into 0.1 nm layers. In the sliced slab, we show the average charge density per unit surface area and then scale to the absolute value of the surface charge density of the electrode. The results are shown in Figure 5. For small electrical voltages, the corresponding groups of these same charges and counter-charges nearest the electrode provide the higher values than the absolute charge density of the electrodes. This condition is known as the overscreening effect, which was first proposed by Kornyshev[31] and has been extensively discussed in many

papers.[31−40] In our system, this type of overscreening structure evidently differs from the common overscreening. Considering the small electrical voltages used in our system, regardless of the location at the anode or cathode, the first screening layer nearest the electrode is always a small negative charge layer; this layer is followed by two larger overscreening layers with separate positive and negative charge. This phenomenon diminishes until electroneutrality is reached after a set of screening of the counter charges. As shown in Figure 5c and d, the overscreening effect persists, particularly at the anode, even at high electrical voltages. Overscreening can be easily observed at the anode because the anion is smaller than the cation and can therefore form a dense ion-rich region in which to screen anode surface charges. This overscreening effect gradually decreases with increasing applied electrical potential. In Figure 5d, the values of the positive screening charges of the cation layer at 12.7 nm are very similar to the absolute values of the negative surface charges of the cathode. At high electrical potentials, the first screening layers at the anode and the cathode correspond to a net anion layer and a net cation layer, respectively. This finding can be proven by the disappearances of the *P* atom number density of the anion at high negative potentials and the *N* atom number density of the cation at high positive potentials, as shown in Figure 4. The corresponding snapshots of the EDL structures in Figure 7 could also confirm these findings.

As shown in Figure 5d, a net anion layer in the first screening layer corresponds to a sandwich-type charged structure (i.e., a net positive charge layer located between two net negative charge layers), whereas a net cation layer corresponds to a net positive charge layer. A sandwich-type structure of the charge layers is rooted in three separate density peaks of the PF_6 anion in Figure 3b. The positively charged layer is induced by the positive atom charge of *P*, whereas the negatively charged layers are produced by the negative atom charge of *F* in the anion. At moderately high potentials, the first screening layer consists of anions and cations, which are both strongly adsorbed on the same plane parallel to the electrode surfaces. Furthermore, the imidazolium ring of the cation in the first screening layer lies on the electrode surface and is closer to the electrode surface than the anion. This condition results in a decrease in the first-negative charge layer and an increase in the middle-positive charge layer in the sandwich structure. This strong adsorption screening layer also explains the severe overscreening effect observed at small electrical voltages. Considering overscreening effects in the first screening layer, the next layer must have a net positive or negative charge to compensate the overscreening charge of the first layer. At small electrical potentials, electrical potential differences induced by overscreening are even higher than that of the compact layer of the EDL. This finding can be seen in Figure 6, which describes Poisson potential profiles across the *z* axis in the simulation cell. In Figure 6a, the location of the first potential peak between 0.7 and 0.8 nm near the anode corresponds accurately to the first screening layer location in Figure 5a. Similar results of potential peak location corresponding to the screening layer location can be observed at the cathode in Figures 5 and 6. These contrastive results clearly indicate that the overscreening layer on the electrode surface results in an extra potential difference at the anode and cathode. Especially under small absolute values of electrode charge, this extra potential difference may be higher than the potential difference induced by the compact layer. Apparently, two primary screening ion layers were induced by this overscreening effect adjacent to the electrode surface. In Figure 6, the Poisson potentials at the anode and cathode always oscillate two potential peaks and then gradually decay to a fixed potential. This potential difference induced by the overscreening effect decreases following the increase in electrode surface charge. As shown in Figure 6d, the contribution of the potential difference induced by the overscreening effect is extremely small.

Representative snapshots of the ion layer structure in the compact and intermediate layers of the EDL are shown in Figure 7 to aid the interpretation of the ion layer structures in Figures 5 and 6. The cations and anions are strongly adsorbed in the same compact layer parallel to the electrode surface near the pzc. The cation alkyl chain and imidazolium ring both lie on the electrode surface. This also can be confirmed by the analysis of the orientation of imidazolium ring and the alkyl chain at the different electrical potentials (see Figure S9 in Supporting Information). The number of cations in the compact layer of the EDL is higher than the number of anions in the same layer. This finding indicates a net cation adsorption effect on the Au(100) electrode surface (Figure 7d). A similar cation adsorption structure has been observed in a series of other experimental observations[24−26,64] and simulations on the same IL.[38,41,53,54] The strong adsorption layer has a net positive charge that is higher than the absolute value of the entire electrode surface charge under small applied electrical potentials. Thus, the overscreening effect gradually decreases following the increase in applied electrical potential. At high electrical potentials, the compact layer of the EDL changes to a net counter-charge layer (Figure 7a and g).

3.4. Surface Charge and Electric Voltage. Kornyshev's[31−33] mean-field theory of IL EDLs predicted that the electrode surface charge density increases at high potentials as $|\sigma| \propto |U|^{1/2}$ and the differential capacitance correspondingly decreases as $C \propto |U|^{-1/2}$. This behavior is considered as lattice saturation, during which no more ions can be packed within the single layer near the surface and thus the thickness of EDL can grow to accumulate sufficient ions and compensate the high charge on the electrode.

In Figure 8, the electrode charge clearly exhibits a linear dependence on the square root of the potentials within the range of 4.0−11.0 V, thereby following the expected theoretical prediction of the differential capacitance $C \propto |U|^{-1/2}$ for the highly charged electrode surface (see Supporting Information). Our simulation results are in good agreement with other molecular dynamics simulation results and mean-field theory of ILs.[31−37] At a lower potential range, the electrical potential presents a slower increase than $|U|^{1/2}$, which indicates that the ions in the first screening layer (compact layer) on the electrode surfaces are not overcrowded and therefore may rearrange. At higher than 4.0 V, it seems that the compact layer gradually changes into a net cation or anion layer. However, it is not true for the ILs at the Au(100) electrodes, since the cation−anion structure in the double layer is not typically overcrowding in our system. This can be further analyzed by the number density distribution in Figure 9. At anode, even the electric potential attains 4.85 V, there is a little cation retaining ion adsorption at the positive electrode surface. In Figure 9 (a−c), the cations within the first ion layer gradually decrease and the anions within the first ion layer retains an unchangeable number density distribution by increasing the absolute electric potentials at anode. Meanwhile, anions in the second layer are slowly away from the anode surface. These associated effects of

the decreased first cation layer distribution and the removed second anion layer may finally produce a "quasi-overcrowding" effect at the anode, that is, a linear correlation of the electrode charge density versus the square root of electrical potential. In Figure 9d, at a very large electrical potential, a typical overcrowding effect for the thickness increase of anion layer was presented at the anode. Differing from the anode, the anions were completely pushed away from the cathode at −3.9 V in Figure 9b. Above −3.9 V, the typical overcrowding of the anion layer thickness increase was found in Figure 9c and d.

By combination of the number density analysis and the σ-$U^{1/2}$ dependence in Figure 8, we obtained the transition electrical potential of the overscreening to overcrowding is about 4.0 V. Though there is a little difference in the transition electrical potential between the cathode and the anode, this value of transition potential is close to the simulation result of Bazant et al.[45] for the same type of transition. However, Borodin et al.[35] found that higher potentials (about 15 V) are required for IL-graphite electrode systems to shift from overscreening to overcrowding. This transition potential difference may be attributed to the higher interaction energy between the Au(100) electrode and ions compared with the binding energy of our cation−anion system. This result is very different from the close interaction energies observed between the ions-graphite and the cations-anions in the IL-graphite system.

4. CONCLUSIONS

Molecular dynamics simulations of IL $BmimPF_6$ in contact with single crystalline Au(100) electrodes were performed as a function of electrical potential. These simulations enable us to establish clear molecular insights into the changes in the ion structure on electrode surfaces as well as the behavior of the differential capacitance under changing electrical potentials. Our simulations revealed that strong ion adsorption interactions between the Au electrode surface and ions adsorption layer mainly determine the behavior of differential capacitance. This strong adsorption layer results in overscreening effects on the first screening layer and induces the pzc to move toward positive potentials. We further observed that the potential required to transition from overscreening to overcrowding is about 4.0 V. This transition potential may be attributed to the higher interaction energy between the Au(100) electrode and ions compared with the binding energy of cation−anion in our system.

■ ASSOCIATED CONTENT

Supporting Information

Detailed force field parameters, mass density of ionic liquid at Au(100) electrode, detailed introduction of the differential capacitance and integral capacitance calculations, potential of the zero charge, charge density profiles, and orientation of cations in the EDL at different applied electrical potential. This material is available free of charge via the Internet at http://pubs.acs.org.

■ AUTHOR INFORMATION

Corresponding Author

*Tel.: +86-021-59558905. Fax: +86-021-59558905. Email: wuguozhong@sinap.ac.cn.

Notes

The authors declare no competing financial interest.

■ ACKNOWLEDGMENTS

This work was supported by the National Science Foundations of China (11079007, 20103040, and 21173002), the Anhui Provincial Natural Science Foundation (1408085QB37), and the Natural Science Foundation of the Anhui Higher Education Institutions of China (KJ2012Z329).

■ REFERENCES

(1) Welton, T. Room-Temperature Ionic Liquids. Solvents for Synthesis and Catalysis. *Chem. Rev.* **1999**, *99*, 2071−2084.
(2) Rogers, R. D.; Seddon, K. R. Ionic Liquids—Solvents of the Future? *Science.* **2003**, *302*, 792−793.
(3) Robinson, J.; Osteryoun, R. A. An Electrochemical and Spectroscopic Study of Some Aromatic Hydrocarbons in the Room Temperature Molten Salt System Aluminum Chloride-*n*-butylpyridinium Chloride. *J. Am. Chem. Soc.* **1979**, *101*, 323−327.
(4) Mezger, M.; Schröder, H.; Reichert, H.; Schramm, S.; Okasinski, J. S.; Schröder, S.; Honkimäki, V.; Deutsch, M.; Ocko, B. M.; Ralston, J.; Rohwerder, M.; Stratmann, M.; Dosch, H. Molecular Layering of Fluorinated Ionic Liquids at a Charged Sapphire (0001). *Surf. Sci.* **2008**, *322*, 424−428.
(5) Wang, P.; Bernard, W.; Robin, H.; Moser, J.; Teuscher, J.; Kantlehner, W.; Mezger, J.; Stoyanov, E. V.; Shaik, M. Z.; Michael, G. Charge Separation and Efficient Light Conversion in Sensitized Mesoscopic Solar Cells Based on Binary Ionic Liquids. *J. Am. Chem. Soc.* **2005**, *127*, 6850−6856.
(6) Largeot, C.; Portet, C.; Chmiola, J.; Taberna, P. L.; Gogotsi, Y.; Simon, P. Relation between the Ion Size and Pore Size for an Electric Double-Layer Capacitor. *J. Am. Chem. Soc.* **2008**, *130*, 2730−2731.
(7) Chmiola, J.; Yushin, G.; Gogotsi, Y.; Portet, C.; Simon, P.; Taberna, P. L. Anomalous Increase in Carbon Capacitance at Pore Sizes Less Than 1 Nanometer. *Science* **2006**, *313*, 1760−1763.
(8) Crowhurst, L.; Lancaster, N. L.; Arlandis, J. M. P.; Welton, T. Manipulating Solute Nucleophilicity with Room Temperature Ionic Liquids. *J. Am. Chem. Soc.* **2004**, *126*, 11549−11555.
(9) Hayes, R.; Borisenko, N.; Tam, M. K.; Howlett, P. C.; Endres, F.; Atkin, R. Double Layer Structure of Ionic Liquids at the Au(111) Electrode Interface: An Atomic Force Microscopy Investigation. *J. Phys. Chem. C* **2011**, *115*, 6855−6863.
(10) Nanjundiah, C.; McDevitt, S. F.; Koch, V. R. Differential Capacitance Measurements in Solvent-Free Ionic Liquids at Hg and C Interfaces. *J. Electrochem. Soc.* **1997**, *144*, 3392−3397.
(11) Alam, M. T.; Islam, M. M.; Okajima, T.; Ohsaka, T. Measurements of Differential Capacitance at Mercury/Room-Temperature Ionic Liquids Interfaces. *J. Phys. Chem. C* **2007**, *111*, 18326−18333.
(12) Alam, M. T.; Islam, M. M.; Okajima, T.; Ohsaka, T. Capacitance Measurements in a Series of Room-Temperature Ionic Liquids at Glassy Carbon and Gold Electrode Interfaces. *J. Phys. Chem. C* **2008**, *112*, 16600−16608.
(13) Alam, M. T.; Islam, M. M.; Okajima, T.; Ohsaka, T. Electrical Double-Layer in Ionic Liquids: An Understanding of the Unusual Capacitance−Potential Curve at a Nonmetallic Electrode. *J. Phys. Chem. C* **2009**, *113*, 3386−3389.
(14) Silva, F.; Gomes, C.; Figueiredo, M.; Costa, R.; Martins, A.; Pereira, C. M. The Electrical Double Layer at the [Bmim][PF6] Ionic Liquid/Electrode Interface-Effect of Temperature on the Differential Capacitance. *J. Electroanal. Chem.* **2008**, *622*, 153−160.
(15) Locket, V.; Sedev, R.; Ralston, J.; Horne, M.; Rodopoulos, T. Differential Capacitance of the Electrical Double Layer in Imidazolium-Based Ionic Liquids: Influence of Potential, Cation Size, and Temperature. *J. Phys. Chem. C* **2008**, *112*, 7486−7495.
(16) Locket, V.; Horne, M.; Sedev, R.; Rodopoulos, T.; Ralston, J. Differential Capacitance of the Double Layer at the Electrode/Ionic Liquids Interface. *Phys. Chem. Chem. Phys.* **2010**, *12*, 12499−12512.
(17) Drüschler, M.; Huber, B.; Passerini, S.; Roling, B. Hysteresis Effects in the Potential-Dependent Double Layer Capacitance of

Room Temperature Ionic Liquids at a Polycrystalline Platinum Interface. *J. Phys. Chem. C* **2010**, *114*, 3614−3617.
(18) El Abedin, S. Z.; Saad, A. Y.; Farag, H. K.; Borisenko, N.; Liu, Q. X.; Endres, F. Electrodeposition of Selenium, Indium, and Copper in an Air- and Water-Stable Ionic Liquid at Variable Temperatures. *Electrochim. Acta* **2007**, *52*, 2746−2754.
(19) Drüschler, M.; Borisenko, N.; Wallauer, J.; Winter, C.; Huber, B.; Endres, F.; Roling, B. New Insights into the Interface between a Single-Crystalline Metal Electrode and an Extremely Pure Ionic Liquid: Slow Interfacial Process and the Influence of Temperature on Interfacial Dynamics. *Phys. Chem. Chem. Phys.* **2012**, *14*, 5090−5099.
(20) Gnahm, M.; Pajkossy, T.; Kolb, D. M. The Interface between Au(111) and an Ionic Liquid. *Electrochim. Acta* **2010**, *55*, 6212−6217.
(21) Gnahm, M.; Müller, C.; Répánszki, R.; Pajkossy, T.; Kolb, D. M. The Interface between Au(100) and 1-Butyl-3-Methyl-Imidazolium Hexafluorophosphate. *Phys. Chem. Chem. Phys.* **2011**, *13*, 11627−11633.
(22) Pajkossy, T.; Kolb, D. M. The Interfacial Capacitance of Au(100) in an Ionic Liquid, 1-Butyl-3-Methyl-Imidazolium hexafluorophosphate. *Electrochem. Commun.* **2011**, *13*, 284−286.
(23) Su, Y. Z.; Fu, Y. C.; Yan, J. W.; Chen, Z. B.; Mao, B. W. Double Layer of Au(100)/Ionic Liquid Interface and Its Stability in Imidazolium-Based Ionic Liquids. *Angew. Chem., Int. Ed.* **2009**, *48*, 5148−5151.
(24) Su, Y. Z.; Fu, Y. C.; Wei, Y. M.; Yan, J. W.; Mao, B. W. The Electrode/Ionic Liquid Interface: Electric Double Layer and Metal Electrodeposition. *ChemPhysChem* **2010**, *11*, 2764−2778.
(25) Atkin, R.; El Abedin, S. Z.; Hayes, R.; Gasparotto, L. H. S.; Borisenko, N.; Endres, F. AFM and STM Studies on the Surface Interaction of [BMP]TFSA and [EMIM]TFSA Ionic Liquids with Au(111). *J. Phys. Chem. C* **2009**, *113*, 13266−13272.
(26) Endres, F.; Borisenko, N.; El Abedin, S. Z.; Hayes, R.; Atkin, R. The Interface Ionic Liquids/Electrodes: In Situ STM and AFM Measurements. *Faraday Discuss.* **2012**, *154*, 221−233.
(27) Hayes, R.; Warr, G. G.; Atkin, R. At the Interface: Solvation and Designing Ionic Liquids. *Phys. Chem. Chem. Phys.* **2010**, *12*, 1709−1723.
(28) Atkin, R.; Warr, G. G. Structure in Confined Room-Temperature Ionic Liquids. *J. Phys. Chem. C* **2007**, *111*, 5162−5168.
(29) Lauw, Y.; Horne, M. D.; Rodopoulos, T.; Lockett, V.; Akgun, B.; Hamilton, W. A.; Nelson, A. R. Structure of $[C_4mpyr][NTf_2]$ Room-Temperature Ionic Liquid at Charged Gold Interfaces. *Langmuir* **2012**, *28*, 7374−7381.
(30) Chen, S.; Kobayashi, K.; Kitaura, R.; Miyata, Y.; Shinohara, H. Direct HRTEM Observation of Ultrathin Freestanding Ionic Liquid Film on Carbon Nanotube Grid. *ACS Nano* **2011**, *5*, 4902−4908.
(31) Kornyshev, A. A. Double-Layer in Ionic Liquids: Paradigm Change? *J. Phys. Chem. B* **2007**, *111*, 5545−5557.
(32) Fedorov, M. V.; Kornyshev, A. A. Ionic Liquid Near A Charged Walls: Structure and Capacitance of Electrical Double Layer. *J. Phys. Chem. B* **2008**, *112*, 11868−11872.
(33) Fedorov, M. V.; Georgi, N.; Kornyshev, A. A. Double Layer in Ionic Liquids: The Nature of the Camel Shape of Capacitance. *Electrochem. Commun.* **2010**, *12*, 296−299.
(34) Lauw, Y.; Horne, M. D.; Rodopoulos, T.; Nelson, A.; Leermakers, F. A. M. Electrical Double-Layer Capacitance in Room Temperature Ionic Liquids: Ion-Size and Specific Adsorption Effects. *J. Phys. Chem. B* **2010**, *114*, 11149−11154.
(35) Vatamanu, J.; Borodin, O.; Smith, G. D. Molecular Insights into the Potential and Temperature Dependences of the Differential Capacitance of a Room-Temperature Ionic Liquid at Graphite Electrodes. *J. Am. Chem. Soc.* **2010**, *132*, 14825−14833.
(36) Feng, G.; Huang, J. S.; Sumpter, B. G.; Meunier, V.; Qiao, R. A "Counter-Charge Layer in Generalized Solvents" Framework for Electrical Double Layers in Neat and Hybrid Ionic Liquid Electrolytes. *Phys. Chem. Chem. Phys.* **2011**, *13*, 14723−14734.
(37) Wu, P.; Huang, J. S.; Meunier, V.; Sumpter, B. G.; Qiao, R. Complex Capacitance Scaling in Ionic Liquids-Filled Nanopores. *ACS Nano* **2011**, *5*, 9044−9051.
(38) Kislenko, S. A.; Samoylov, I. S.; Amirov, R. H. Molecular Dynamics Simulation of the Electrochemical Interface between a Graphite Surface and the Ionic Liquid $[BMIM][PF_6]$. *Phys. Chem. Chem. Phys.* **2009**, *11*, 5584−5590.
(39) Merlet, C.; Rotenberg, B.; Madden, P. A.; Taberna, P.; Simon, P.; Gogotsi, Y.; Salanne, M. On the Molecular Origin of Supercapacitance in Nanoporous Carbon Electrodes. *Nat. Mater.* **2012**, *11*, 306−310.
(40) Merlet, C.; Salanne, M.; Rotenberg, B.; Madden, P. A. Imidazolium Ionic Liquid Interfaces with Vapor and Graphite: Interfacial Tension and Capacitance from Coarse-Grained Molecular Simulations. *J. Phys. Chem. C* **2011**, *115*, 16613−16618.
(41) Wang, S.; Li, S.; Cao, Z.; Yan, T. Y. Molecular Dynamic Simulations of Ionic Liquids at Graphite Surface. *J. Phys. Chem. C* **2010**, *114*, 990−997.
(42) Oldham, K. B. A Gouy−Chapman−Stern Model of the Double Layer at a (Metal)/(Ionic Liquid) Interface. *J. Electroanal. Chem.* **2008**, *613*, 131−138.
(43) Henderson, D.; Wu, J. Z. Electrochemical Properties of the Doubl Layer of an Ionic Liquid Using a Dimer Model Electrolyte and Density Functional Theory. *J. Phys. Chem. B* **2012**, *116*, 2520−2525.
(44) Lynden-Bell, R. M.; Frolov, A. I.; Fedorov, M. V. Electrode Screening by Ionic Liquids. *Phys. Chem. Chem. Phys.* **2012**, *14*, 2693−2701.
(45) Bazant, M. Z.; Storey, B. D.; Kornyshev, A. A. Double Layer in Ionic Liquids: Overscreening versus Crowding. *Phys. Rev. Lett.* **2011**, *106*, 046102.
(46) Lamperski, S.; Outhwaite, C. W.; Bhuiyan, L. B. The Electric Double-Layer Differential Capacitance at and Near Zero Surface Charge for a Restricted Primitive Model Electrolyte. *J. Phys. Chem. C* **2009**, *113*, 8925.
(47) Lamperski, S.; Henderson, D. Simulation Study of Capacitance of the Electrical Double Layer of an Electrolyte Near a Highly Charged Electrode. *Mol. Simul.* **2011**, *37*, 264−268.
(48) Tazi, S.; Salanne, M.; Simon, C.; Turq, P.; Pounds, M.; Madden, P. A. Potential-Induced Ordering Transition of the Adsorbed Layer at the Ionic Liquid/Electrified Metal Interface. *J. Phys. Chem. B* **2010**, *114*, 8453−8459.
(49) Jiang, D.; Jin, Z.; Henderson, D.; Wu, J. Solvent Effect on the Pore-Size Dependence of an Organic Electrolyte Supercapacitor. *J. Phys. Chem. Lett.* **2012**, *3*, 1727−1731.
(50) Xing, L.; Vatamanu, J.; Smith, G. D.; Bedrov, D. Nanopatterning of Electrode Surfaces As a Potential Route To Improve the Energy of Electric Double-Layer Capacitors: Insight from Molecular Simulations. *J. Phys. Chem. Lett.* **2012**, *3*, 1124−1129.
(51) Jorgensen, W. L.; Maxwell, D.; Tirado-Rives, J. Development and Testing of the OPLS All-Atom Force Field on Conformational Energetics and Properties of Organic Liquids. *J. Am. Chem. Soc.* **1996**, *118*, 11225−11236.
(52) Canongia Lopes, J. N.; Deschamps, J.; Pódua, A. A. H. Modeling Ionic Liquids Using a Systematic All-Atom Force Field. *J. Phys. Chem. B* **2004**, *108*, 2038−2047.
(53) Sha, M. L.; Zhang, F. C.; Wu, G. Z.; Fang, H. P.; Wang, C. L.; Chen, S. M.; Zhang, Y.; Hu, J. Ordering Layers of $[bmim][PF_6]$ Ionic Liquid on Graphite Surfaces: Molecular Dynamics Simulation. *J. Chem. Phys.* **2008**, *128*, 134504.
(54) Sha, M. L.; Wu, G. Z.; Dou, Q.; Tang, Z. F.; Fang, H. P. Double-Layer Formation of $[Bmim]$ $[PF_6]$ Ionic Liquid Triggered by Surface Negative Charge. *Langmuir* **2010**, *26*, 12667−12675.
(55) Yeh, I.; Berkowitz, M. Ewald Summation for Systems with Slab Geometry. *J. Chem. Phys.* **1999**, *111*, 3155−3162.
(56) Yeh, I.; Berkowitz, M. Effects of the Polarizability and Water Density Constraint on the Structure of Water Near Charged Surfaces: Molecular Dynamics Simulations. *J. Chem. Phys.* **2000**, *112*, 10491−10495.
(57) Neves, R. S.; Motheo, A. J.; Fartaria, R. P. S.; Fernandes, F. M. S. Modelling Water Adsorption on Au(210) Surfaces, II. Monte Carlo Simulations. *J. Electroanal. Chem.* **2008**, *612*, 179−185.

(58) Philpott, M. R.; Glosli, J. N. Electric Potential Near a Charged Metal Surface in Contact with Aqueous Electrolyte. *J. Electroanal. Chem.* **1996**, *409*, 65−72.
(59) Guidelli, R.; Schmickler, W. Recent Developments in Models for the Interface between a Metal and an Aqueous Solution. *Electrochim. Acta* **2000**, *45*, 2317−2338.
(60) Heinz, H.; Vaia, R. A.; Farmer, B. L.; Naik, R. R. Accurate Simulation of Surfaces and Interfaces of Face-Centered Cubic Metals Using 12−6 and 9−6 Lennard-Jones Potentials. *J. Phys. Chem. C* **2008**, *112*, 17281−17290.
(61) Gu, Z.; Brennecke, J. F. Volume Expansivities and Isothermal Compressibilities of Imidazolium and Pyridinium-Based Ionic Liquids. *J. Chem. Eng. Data* **2002**, *47*, 339−345.
(62) Van Der Spoel, D.; Lindahl, E.; Hess, B.; Groenhof, G.; Mark, A. E.; Berendsen, H. J. Gromacs: Fast, Flexible, and Free. *J. Comput. Chem.* **2005**, *26*, 1701−1718.
(63) Hess, B.; Kutzner, C.; Van Der Spoel, D.; Lindahl, E. GROMACS 4: Algorithms for Highly Efficient, Load-Balanced, and Scalable Molecular Simulation. *J. Chem. Theory Comput.* **2008**, *4*, 435−447.
(64) Baldelli, S. Surface Structure at the Ionic Liquid-Electrified Metal Interface. *Acc. Chem. Res.* **2008**, *41*, 421−431.